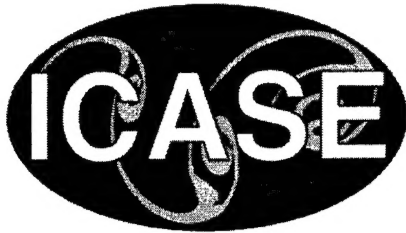NASA/CR-2001-211060
ICASE Report No. 2001-24

Schiestel's Derivation of the Epsilon Equation and Two Equation Modeling of Rotating Turbulence

Robert Rubinstein
NASA Langley Research Center, Hampton, Virginia

Ye Zhou
Lawrence Livermore National Laboratory, Livermore, California

ICASE
NASA Langley Research Center
Hampton, Virginia

Operated by Universities Space Research Association

National Aeronautics and
Space Administration

Langley Research Center
Hampton, Virginia 23681-2199

September 2001

20010927 111

SCHIESTEL'S DERIVATION OF THE EPSILON EQUATION AND TWO EQUATION MODELING OF ROTATING TURBULENCE

ROBERT RUBINSTEIN* AND YE ZHOU†

Abstract. As part of a more general program of developing multiple-scale models of turbulence, Schiestel suggested a derivation of the homogeneous part of the dissipation rate transport equation. Schiestel's approach is generalized to rotating turbulence. The resulting model reproduces the main features observed in decaying rotating turbulence.

Key words. dissipation rate equation, rotating turbulence, two-equation turbulence models, multiple-scale turbulence models

Subject classification. Fluid Mechanics

1. Introduction. The dissipation rate transport equation continues to resist systematic derivation, either from the governing equations or even from statistical closures. Much of the closure-based work is summarized in [1]; more recent work is summarized in [2]. In many respects, the most successful derivation of the ϵ transport equation is due to Schiestel [3]. Among the successes of the derivation is a rather good value $C_{\epsilon 1} = 1.5$ and the demonstration that necessarily, $C_{\epsilon 2} > C_{\epsilon 1}$.

It is well-known that the derivation of the ϵ equation in rotating turbulence encounters additional difficulties because rotation does not appear explicitly in the exact transport equation for the dissipation rate. Instead, the effect of rotation is indirect, entering only through quantities like the turbulent time-scale. In the present work, the ϵ transport equation is treated by combining Schiestel's arguments with the phenomenology for rotating turbulence of Zhou [4]. The most direct generalization of the argument of [3] leads to a rotation-sensitized ϵ equation with the same form as the standard ϵ equation, but with an increased value of $C_{\epsilon 2}$; a model of this type was proposed by Okamoto [5]. A simple modification of the argument of [3] yields instead a model of the form first proposed by Bardina *et al* [6]. The implications of these models for decaying rotating turbulence are discussed.

2. Review of Schiestel's derivation. We begin with a split-spectrum model of high Reynolds number turbulence,

$$
(2.1) \qquad E(\kappa) = \begin{cases} C\kappa^2 & \text{if } \kappa < \kappa_0 \\ C_K \epsilon^{2/3} \kappa^{-5/3} & \text{if } \kappa > \kappa_0 \end{cases}
$$

In Eq. (2.1), κ_0 is the inverse integral scale of turbulence which marks the transition between the inertial range and the large scales. Eq. (2.1) is a special case of the models introduced in [3] in connection with multiple-scale turbulence models. This is no more than a schematic model of the actual energy spectrum; however, as stressed in [3] and [7], to derive a two-equation model, it is essential that the spectrum be

parametrized in some simple way. Use of a more complex model like the von Kàrmàn spectrum would lead to essentially the same results.

Denote the energy in the inertial range by

$$(2.2) \qquad k = \frac{3}{2} C_K \epsilon^{2/3} \kappa_0^{-2/3}$$

and the energy in the large scales by

$$(2.3) \qquad k_0 = \frac{1}{3} C \kappa_0^3$$

Assume that the spectral descriptors in Eq. (2.1) are functions of time: $\epsilon = \epsilon(t)$ and $\kappa_0 = \kappa_0(t)$. It follows from Eq. (2.2) that

$$(2.4) \qquad \dot{k} = C_K (\epsilon^{-1/3} \kappa_0^{-2/3} \dot{\epsilon} - \epsilon^{2/3} \kappa_0^{-5/3} \dot{\kappa}_0)$$

This equation does not lead to the desired ϵ equation directly, because it contains the new unknown $\dot{\kappa}_0$.

To solve this problem, we postulate

$$(2.5) \qquad \dot{\kappa}_0 = -\beta \frac{\epsilon}{E(\kappa_0)}$$

based on a very similar proposal in [3]. In view of Eq. (2.1), Eq. (2.5) is equivalent to

$$(2.6) \qquad \dot{\kappa}_0 / \kappa_0 = -\frac{3}{2} \beta \epsilon / k$$

Then Eqs. (2.4)–(2.6) give

$$(2.7) \qquad \dot{k} = \frac{2}{3} \frac{k}{\epsilon} \dot{\epsilon} - \beta \epsilon$$

which can be re-arranged as

$$(2.8) \qquad \dot{\epsilon} = \frac{3}{2} \frac{\epsilon}{k} P - \frac{3}{2} (1 + \beta) \frac{\epsilon^2}{k}$$

with a rather good value for $C_{\epsilon 1}$ and a value for $C_{\epsilon 2}$ which depends on the choice of β. This result is essentially Eq. (27) of [3].

Following Reynolds [8], the constant β can be fixed by appealing to the behavior of the large scales of motion during decay. Differentiation of Eq. (2.3) gives

$$(2.9) \qquad \frac{\dot{k}_0}{k_0} = 3 \frac{\dot{\kappa}_0}{\kappa_0}$$

and differentiation of Eq. (2.2) gives

$$(2.10) \qquad \frac{\dot{k}}{k} = \frac{2}{3} \frac{\dot{\epsilon}}{\epsilon} - \frac{2}{3} \frac{\dot{\kappa}_0}{\kappa_0}$$

Assuming that decay is self-similar, so that

$$(2.11) \qquad \frac{\dot{k}}{k} = \frac{\dot{k}_0}{k_0}$$

Eqs. (2.9)–(2.11) lead as usual to

$$(2.12) \qquad \frac{\dot{\epsilon}}{\epsilon} = -\frac{11}{6} \frac{\epsilon}{k}$$

2

corresponding, in Eq. (2.8), to $\beta = 2/9$.

It would seem that this argument solves the problem of deriving the homogeneous ϵ transport equation, since it gives the values $C_{\epsilon 1} = 3/2$ and $C_{\epsilon 2} = 11/6$. But one can object that the assumption Eq. (2.6) is another way of stating the final result: this equation states that the integral scale κ_0^{-1} satisfies a transport equation in which the production term is absent. Indeed, writing

$$(2.13) \qquad \frac{d}{dt}\frac{k^{3/2}}{\epsilon} = \frac{3}{2}\frac{k^{1/2}}{\epsilon}\dot{k} - \frac{k^{3/2}}{\epsilon^2}\dot{\epsilon}$$

and substituting

$$
\begin{aligned}
\dot{k} &= P - \epsilon \\
(2.14) \qquad \dot{\epsilon} &= \frac{\epsilon}{k}[C_{\epsilon 1}P - C_{\epsilon 2}\epsilon]
\end{aligned}
$$

leads to

$$(2.15) \qquad \frac{d}{dt}\frac{k^{3/2}}{\epsilon} = (\frac{3}{2} - C_{\epsilon 1})\frac{k^{1/2}}{\epsilon}P + (C_{\epsilon 2} - \frac{3}{2})k^{1/2}$$

which shows that the absence of a production term in the length-scale transport equation is equivalent to $C_{\epsilon 1} = 3/2$.

The injection of energy at large scales can certainly cause the integral scale to increase; at the same time, turbulence production might be expected to it to decrease through the enhancement of small scales. Eq. (2.5) states the dominance of the first process over the second. Although the validity of this approximation is uncertain, the success of the argument is undeniable, and it seems reasonable to ask what conclusions will result if the same argument is applied to another problem.

3. Rotating turbulence. To derive an ϵ equation for rotating turbulence, we will combine the arguments of the previous section with Zhou's phenomenological model of rotating turbulence [4]. Briefly, this model postulates that strong rotation replaces the nonlinear time scale k/ϵ by the inverse rotation rate Ω^{-1}; closure theories lead to

$$(3.1) \qquad \epsilon \sim \kappa^4 T E(\kappa)^2$$

where by hypothesis, $T \propto \Omega^{-1}$, hence

$$(3.2) \qquad E(\kappa) = C_K^{\Omega}\sqrt{\epsilon\Omega}\kappa^{-2}$$

For notational simplicity, Ω will denote twice the absolute value of the rotation rate throughout.

Adding a model for the large scales, we obtain the analog of the split-spectrum model of Eq. (2.1) for rotating turbulence,

$$(3.3) \qquad E(\kappa) = \begin{cases} C\kappa^2 & \text{if } \kappa < \kappa_0 \\ C_K^{\Omega}\sqrt{\Omega\epsilon}\kappa^{-2} & \text{if } \kappa > \kappa_0 \end{cases}$$

Again, we have the energy of the large scales,

$$(3.4) \qquad k_0 = \frac{1}{3}C\kappa_0^3$$

and the inertial range energy

$$(3.5) \qquad k = C_K^{\Omega}\sqrt{\Omega\epsilon}\kappa_0^{-1}$$

3

Note that the definition of the integral scale implied by Eq. (3.5) differs from the non-rotating result Eq. (2.2).

Following Schiestel, we differentiate Eq. (3.5) to obtain

$$(3.6) \qquad \frac{\dot{k}}{k} = \frac{1}{2}\frac{\dot{\epsilon}}{\epsilon} - \frac{\dot{\kappa}_0}{\kappa_0}$$

As before, we must specify an equation for the inverse integral scale κ_0 in order to complete the model.

The simplest possibility is to retain Eq. (2.5). In this case, substitution of the rotation-modified spectrum Eq. (3.2) again leads to Eq. (2.6), but with a new constant of proportionality,

$$(3.7) \qquad \dot{\kappa}_0/\kappa_0 = -\gamma\epsilon/k$$

Following the previous steps, we find instead of Eq. (2.8)

$$(3.8) \qquad \dot{\epsilon} = 2\frac{\epsilon}{k}P - (2+2\gamma)\frac{\epsilon^2}{k}$$

with the definite prediction that $C_{\epsilon 1} = 2$ and $C_{\epsilon 2} > 2$.

The constant γ can be evaluated by assuming that the constant β in Eq. (2.5) is independent of rotation. Tentatively accepting the non-rotating result $\beta = 2/9$ suggested earlier, Eq. (2.5) with the rotation-dependent energy spectrum Eq. (3.2) leads to $\gamma = 2/9$ and to the value $C_{\epsilon 2} = 22/9$. In decaying rotating turbulence, Eq. (3.8) predicts power-law decay in time, but with a smaller exponent than non-rotating turbulence: indeed, following [8], we have

$$(3.9) \qquad k(t) \sim t^{-1/(C_{\epsilon 2}-1)}$$

and the increase in $C_{\epsilon 2}$ due to rotation from 11/6 to 22/9 implies a reduction in the decay rate.

The model of rotating decaying turbulence implied by Eq. (3.8) has been advocated, for example in [5], and more recently in [9]. The value $C_{\epsilon 2} = 22/9$ in rotating turbulence can be compared to the values $C_{\epsilon 2} \approx 2.8$ recommended in [5] and $C_{\epsilon 2} = 8/3$ suggested in [9].

However, the available data is also consistent with the conclusion that in rotating turbulence, energy transfer is suppressed completely, and energy becomes trapped in the largest scales of motion, where it undergoes purely viscous decay. This picture, which is inconsistent with any kind of power-law decay, is advocated for example by [10] and [11]. Which description of decaying rotating turbulence is correct remains controversial; for now, we would like to explore some models which are consistent with the second viewpoint.

The derivation of Eq. (3.2) assumes that the time-scale in strongly rotating turbulence is the inverse rotation rate. This idea suggests replacing Eq. (2.6) by

$$(3.10) \qquad \frac{\dot{\kappa}_0}{\kappa_0} = -\gamma'\Omega$$

in the strong rotation limit. Eqs. (3.6) and (3.10) yield the ϵ equation in the form

$$(3.11) \qquad \dot{\epsilon} = 2\frac{\epsilon}{k}(P - \epsilon) - \gamma'\Omega\epsilon$$

The rotation dependence found in Eq. (3.11) coincides with that of the well-known Bardina model [6]; we argued previously [1] for the strong rotation limit of this model on the basis of simplified closure arguments. Integration of the Bardina model for decaying turbulence in the strong rotation limit gives the results that ϵ decays exponentially in time, but that the kinetic energy approaches a constant; if viscosity is included in the analysis, then the kinetic energy undergoes purely viscous decay.

Although these conclusions are consistent with numerical and experimental observations [10], the assumption Eq. (3.10) underlying the present derivation has the consequence that the integral scale grows exponentially. This was cited in [9] as evidence against the Bardina model itself, although [11] argued that quite different two-point behavior can be consistent with the same single-point model.

The difficulty is not so much with Schiestel's formalism, but with applying Eq. (3.10), an isotropic result, to rotating turbulence. In rotating turbulence, the Taylor-Proudman theorem forces the large scales of motion to be nearly two-dimensional. Consequently, the integral scales parallel and perpendicular to the rotation axis are unequal [10].

It is rather difficult to capture this effect in any isotropic model. But suppose that we combine Eqs. (3.6) and (2.9) to give

$$(3.12) \qquad \frac{\dot{k}}{k} = \frac{1}{2}\frac{\dot{\epsilon}}{\epsilon} - \frac{1}{3}\frac{\dot{k}_0}{k_0}$$

and simply postulate the large rotation limit of Eq. (3.11) for decaying turbulence

$$(3.13) \qquad \frac{\dot{\epsilon}}{\epsilon} = -\gamma'\Omega$$

Then we obtain

$$(3.14) \qquad \frac{\dot{k}}{k} = -\frac{1}{2}\gamma'\Omega - \frac{1}{3}\frac{\dot{k}_0}{k_0}$$

or equivalently,

$$(3.15) \qquad k k_0^{1/3} = k(0)k_0(0)^{1/3}e^{-\gamma'\Omega t/2}$$

instead of the self-similarity postulate Eq. (2.11) for non-rotating turbulence. Unlike the argument leading to Eq. (3.8), which like the derivation for isotropic turbulence assumes that the energy decay of the large scales and the inertial range scales is linked by self-similarity, the present derivation instead allows the dynamics of the large scales and the inertial range scales to be different.

The problem of decaying rotating turbulence is defined by the energy equation together with Eq. (3.13) and either Eq. (3.14) or Eq. (3.15). Numerical integration will be required to solve these equations in general, but it is evident that these equations are consistent with the limits

$$\epsilon = 0$$
$$(3.16) \qquad k = 0$$

while

$$k_0 = \text{const.}$$
$$(3.17) \qquad \kappa_0 = \text{const.}$$

Thus, the kinetic energy in the inertial range vanishes, the energy transfer vanishes, but the kinetic energy in the large scales and the integral scale both approach constants in the absence of viscosity.

Let us summarize the differences between the two dynamic descriptions of rotating decay. Power-law decay, but with a reduced exponent, follows if the decay of both the large-scale energy and the inertial range energy is linked through the self-similarity assumption Eq. (2.11). The alternative description, which leads instead to Eqs. (3.16) and (3.17) allows the large-scale and inertial range energies to evolve independently. The argument also implies that in the long-time limit, viscous dissipation and energy transfer are unequal: energy transfer can vanish, but viscous dissipation is always nonzero.

5

4. Conclusions. Schiestel's derivation of the ϵ transport equation has been generalized to rotating turbulence. By assuming that the basic scale relationship Eq. (2.5) applies to both non-rotating and rotating turbulence, we are led to the ϵ equation in the form Eq. (3.8). This equation implies algebraic decay in time of decaying rotating turbulence with a smaller decay rate than non-rotating turbulence. Replacing Eq. (3.8) with the rotation-dependent hypothesis Eq. (3.10) leads essentially to the Bardina model, which implies a completely different description of rotating decay: the nonlinear energy transfer vanishes and in the absence of viscous effects, energy approaches a constant. By ignoring the two-dimensionality and rotation-independence of the large scales, this argument leads to an incorrect description of the integral scale in decaying rotating turbulence. By modifying Schiestel's argument, the Bardina model is shown to be consistent with saturation of the integral scale.

REFERENCES

[1] R. RUBINSTEIN AND YE ZHOU, *Analytical theory of the destruction terms in dissipation rate transport equations*, Phys. Fluids **8** (1996), p. 3172.

[2] A. CADIOU AND K. HANJALIĆ, *One-point multi-scale turbulence closure derived from a spectral description*, TU Delft Report APTF R/99-11, 1999.

[3] R. SCHIESTEL, *Multiple-time-scale modeling of turbulent flows in one point closures*, Phys. Fluids **30** (1987), p. 722.

[4] YE ZHOU, *A phenomenological treatment of rotating turbulence*, Phys. Fluids **7** (1995), p. 2092.

[5] M. OKAMOTO, *Theoretical turbulence modeling of homogeneous decaying flow in a rotating frame*, J. Phys. Soc. Japan **64** (1995), p. 2854.

[6] J. BARDINA, J. H. FERZIGER, AND R. S. ROGALLO, *Effect of rotation on isotropic turbulence: Computation and modeling*, J. Fluid Mech. **154** (1985), p. 321.

[7] T. CLARK AND C. ZEMACH, *A spectral model applied to homogeneous turbulence*, Phys. Fluids **7** (1995), p. 1674.

[8] W. C. REYNOLDS, *Computation of turbulent flows*, Ann. Rev. Fluid Mech. **8** (1976), p. 183.

[9] V. M. CANUTO AND M. S. DUBOVIKOV, *A dynamical model of turbulence V: The effect of rotation*, Phys. Fluids **9** (1997), p. 2132.

[10] C. CAMBON AND J. SCOTT, *Linear and nonlinear models of anisotropic turbulence*, Ann. Rev. Fluid Mech. **31** (1999), p. 1.

[11] YE ZHOU, C. G. SPEZIALE, AND R. RUBINSTEIN, *Some remarks concerning recent work on rotating turbulence*, Phys. Fluids **10** (1998), p. 3242.

NASA/CR-2001-211061
ICASE Report No. 2001-25
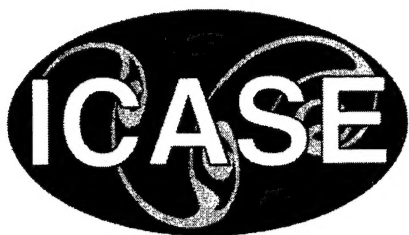
Displacement Models for THUNDER Actuators having General Loads and Boundary Conditions

Robert Wieman, Ralph C. Smith, and Tyson Kackley
North Carolina State University, Raleigh, North Carolina

Zoubeida Ounaies
ICASE, Hampton, Virginia

Jeff Bernd
Ceramic Materials Laboratory, Princeton, New Jersey

ICASE
NASA Langley Research Center
Hampton, Virginia
Operated by Universities Space Research Association

National Aeronautics and
Space Administration

Langley Research Center
Hampton, Virginia 23681-2199

September 2001

DISPLACEMENT MODELS FOR THUNDER ACTUATORS HAVING GENERAL LOADS AND BOUNDARY CONDITIONS

ROBERT WIEMAN*, RALPH C. SMITH†, TYSON KACKLEY‡, ZOUBEIDA OUNAIES§, AND JEFF BERND¶

Abstract. This paper summarizes techniques for quantifying the displacements generated in THUN-DER actuators in response to applied voltages for a variety of boundary conditions and exogenous loads. The PDE models for the actuators are constructed in two steps. In the first, previously developed theory quantifying thermal and electrostatic strains is employed to model the actuator shapes which result from the manufacturing process and subsequent repoling. Newtonian principles are then employed to develop PDE models which quantify displacements in the actuator due to voltage inputs to the piezoceramic patch. For this analysis, drive levels are assumed to be moderate so that linear piezoelectric relations can be employed. Finite element methods for discretizing the models are developed and the performance of the discretized models are illustrated through comparison with experimental data.

Key words. THUNDER actuators, shape model, displacement model

Subject classification. Structures and Materials

1. Introduction. THUNDER actuators offer the capability for generating large strains and forces due to a variety of mechanisms including improved robustness through the manufacturing process and increased electromechanical coupling due to their inherent shape. However, the full capabilities of these actuators have not yet been completely quantified either experimentally or analytically due to their relatively recent genesis and the fact that their behavior differs quite substantially from standard unimorphs or bimorphs. In this paper, we discuss modeling techniques for quantifying the displacements generated by THUNDER actuators in response to applied voltages for a variety of boundary conditions and exogenous loads. The development of corresponding finite element techniques is also addressed and the accuracy of the resulting finite dimensional models is illustrated through comparison with experimental data.

Model development is considered in two steps: (i) the characterization of the actuator shape as a function of the manufacturing process and (ii) the development of a PDE model for the actuator behavior based on Newtonian principles. The first component has been addressed in previous investigations [3] and only those details necessary for the development of the subsequent PDE model will be discussed. As detailed in [3], the characteristic curved shape of THUNDER actuators is due primarily to differing thermal coefficients in the constituent materials, which produce thermal stresses in the combined actuator during cooling, and secondarily to the reorientation of dipoles during repoling. We note that the quantification of strains due to

thermal gradients has been investigated for a variety of applications (e.g., see [2, 4, 5, 6]) with certain aspects having been considered for THUNDER actuators [3, 7]. The quantification of stresses and strains due to repoling is based on domain theory for general ferroelectric materials [8, 9, 12, 13]. Thin shell theory is then employed to develop PDE models which quantify the stresses and displacements throughout the actuator when voltage is applied to the piezoceramic patch. For this analysis, it is assumed that the actuators are operating at low to moderate drive levels for which linear piezoelectric relations are adequate. Techniques for extending these models to regimes in which the piezoelectric response is nonlinear and hysteretic are under investigation and will utilize methods outlined in the concluding remarks.

Because the PDE model is infinite dimensional, approximation techniques must be considered to obtain a finite dimensional model which is appropriate for implementation. This is accomplished through a hybrid finite element approach utilizing linear and cubic Hermite basis functions. This numerical approach differs from that employed in [14], where a NASTRAN model was employed to predict dome heights, in that the finite element method was developed directly for the PDE model used to characterize the physical mechanisms for the actuator. Hence the resulting finite dimensional system incorporates the physical properties associated with the differing constituent materials thus permitting a detailed analysis of various aspects of the actuator dynamics (e.g., stresses or strains at various points along the length of the actuator). This approach also permits direct extension of the numerical method to nonlinear structural models for high drive level dynamics as well as models which incorporate the hysteresis and constitutive nonlinearities inherent to piezoceramic materials at moderate to high drive levels.

The manufacturing conditions for THUNDER are outlined in Section 2 and a model which quantifies the resulting curved shape is summarized in Section 3. The PDE model quantifying the displacements is then presented in Section 4 along with boundary conditions which characterize a variety of experimental setups. The numerical approximation techniques are discussed in Section 5 and examples illustrating the performance of the resulting finite dimensional model are presented in Section 6. Finally, future work, including techniques to extend the model to nonlinear and hysteretic regimes will be outlined in Section 7.

2. Actuator Geometry. THUNDER actuators are typically comprised of a piezoceramic wafer, a metallic backing material, hot melt adhesive layers, and an optional metallic top layer as depicted in Figure 2.1a. As detailed in [3], materials commonly employed for backing layers include aluminum, stainless steel and brass while LaRC-SI is employed as the adhesive.

During the manufacturing process, the materials are placed in a vacuum bag and heated to 325° C under a pressure of 241.3 kPa. During the cooling process, the LaRC-SI solidifies at approximately 270° C and subsequent cooling produces curvature in the actuator due to differing thermal coefficients of the constituent materials. Because the Curie temperature for PZT-5A (350° C) is in the proximity of the manufacturing
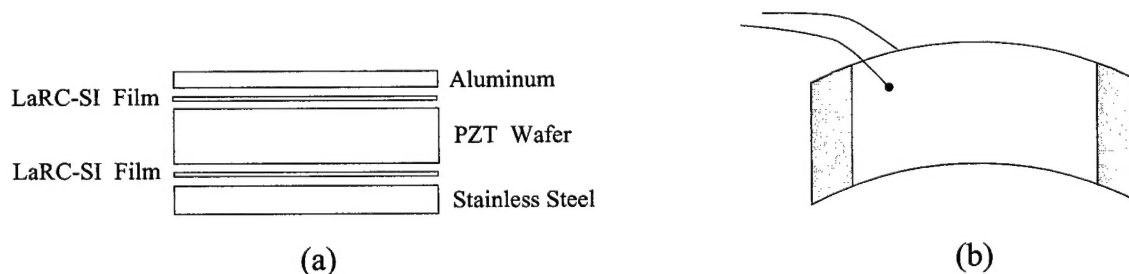

FIG. 2.1. *(a) Components of a THUNDER actuator; (b) Curvature observed in a THUNDER actuator.*

temperature, the final step in the fabrication process is comprised of repoling the material through the application of a sustained DC voltage.

As illustrated in Figure 2.1b, THUNDER actuators have a characteristic dome shape due to the manifestation of differing thermal properties in the PZT and backing material during the cooling process and the rotation of dipoles during repoling. In general, curvature will occur in both component directions in a rectangular actuator; however, for the models developed here, we consider actuators whose width is small as compared with the length so that motion is predominantly in one dimension. Finally, we note that the curvature in the actuators occurs only in regions covered by the piezoceramic patch and the end tabs remain straight.

3. Model for the Manufacturing Process. A necessary step before developing a model which predicts the actuator displacements under various drive conditions is the quantification of the curvature produced in the manufacturing process. We summarize here the characterization of the stresses produced during cooling and repoling which in turn produce the curvature. Details regarding this component of the model can be found in [3].

To accommodate various constructions, we consider actuators with N layers and consider a coordinate system in which the $x - z$ plane corresponds with the outer edge of the backing material and the y-coordinate extends through the thickness of the actuator. The width of the jth layer is denoted by b_j while h_j indicates the thickness of each layer as depicted in Figure 3.1. The Young's modulus and thermal coefficient for the jth layer are respectively denoted by E_j and α_j. The strain at the outer edge of the backing material ($y = 0$) is denoted by ε_0, and κ denotes the curvature at the neutral axis. The change in temperature during the bonding process is indicated by ΔT. To incorporate the strains due to repoling, it is also necessary to employ the Poisson ratio ν and saturation electrostriction λ_s for PZT-5A.

As detailed in [3], the balancing of forces and moments due to thermal and electrostatic stresses yields the linear system

$$(3.1) \qquad\qquad\qquad\qquad A\mathcal{E} = f$$

where $\mathcal{E} = [\varepsilon_0, \kappa]^T$ and

$$(3.2)$$
$$A = \begin{bmatrix} \sum_{j=1}^{N} E_j b_j (h_j - h_{j-1}) & -\frac{1}{2} \sum_{j=1}^{N} E_j b_j (h_j^2 - h_{j-1}^2) \\ \frac{1}{2} \sum_{j=1}^{N} E_j b_j (h_j^2 - h_{j-1}^2) & -\frac{1}{3} \sum_{j=1}^{N} E_j b_j (h_j^3 - h_{j-1}^3) \end{bmatrix}$$

$$f = \begin{bmatrix} \sum_{j=1}^{N} E_j b_j (\alpha_j \Delta T - 3/2\delta\nu\lambda_s)(h_j - h_{j-1}) \\ \frac{1}{2} \sum_{j=1}^{N} E_j b_j (\alpha_j \Delta T - 3/2\delta\nu\lambda_s)(h_j^2 - h_{j-1}^2) \end{bmatrix}.$$

The Kronecker delta, defined by

$$\delta = \begin{cases} 1 \,, & \text{if } y \text{ is in the piezoceramic layer} \\ 0 \,, & \text{otherwise} \end{cases}$$

isolates the electrostatic strains due to repoling to the piezoceramic layer.

To solve for ε_0 and κ, and hence obtain the final radius of curvature $R = 1/\kappa$, it is necessary to obtain values for E_j, α_j for each of the constituent layers in addition to determining $\nu\lambda_s$ for the PZT compound being employed. While the Young's modulus and thermal coefficients are catalogued for various
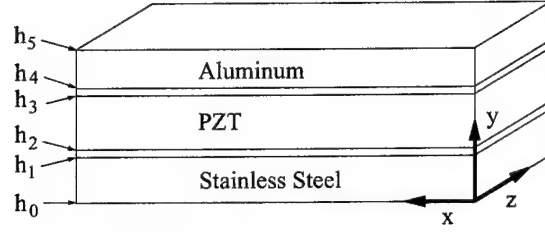
3

FIG. 3.1. *Orientation of the composite THUNDER actuator with five layers.*

PZT compounds and various metallic backing materials, they are temperature-dependent, and not easily quantified, for the LaRC-SI. Hence these parameters are typically estimated through a least squares fit to data for the constituent materials and specific manufacturing conditions under consideration. Details regarding the validity of the model for a variety of materials and geometries can be found in [3].

4. Displacement Model. The system (3.1) quantifies the radius of curvature $R = 1/\kappa$ for differing constituent materials, material dimensions, and manufacturing conditions. In this section, we develop models quantifying displacements produced in the actuators through the input of voltages to the PZT or applied loads. Because end conditions crucially affect the measured displacements, we consider a variety of boundary conditions. Finally, we consider low drive regimes in which the relation between applied voltages and generated strains are approximately linear with minimal hysteresis so that linear piezoelectric relations can be employed.

When modeling the actuator, we consider two regimes. In the first, the entire actuator (including the tabs) is assumed to have the same initial curvature. This approximation to the geometry significantly simplifies the numerical implementation of the model but imposes the assumption that the tabs are initially curved. In the second configuration, only that region covered by PZT is assumed to be initially curved and the end tabs are taken to be flat in the absence of an applied voltage or load. This accurately represents the initial configuration of the actuator after the manufacturing process. One of the objectives when validating the model is to compare the performance of both models and ascertain tab dimensions when the latter model is sufficiently accurate.

4.1. Model 1. We consider initially the model which results from the assumption that the tabs have the same curvature as that portion of the actuator covered by the PZT patch. The radius of curvature is denoted by R (recall that $R = 1/\kappa$ can be predicted using the model summarized in Section 3) and the backing material is assumed to have width b, thickness h, and Young's modulus E. The corresponding parameters for the PZT layer are respectively denoted by b_{pe}, h_{pe} and E_{pe}. The backing material is assumed to extend from $\theta = 0$ to $\theta = L$ and the region $[\gamma_1, \gamma_2]$ covered by the patch is delineated by the characteristic function

(4.1)
$$\chi_{pe} = \begin{cases} 1 & , \gamma_1 \leq \gamma \leq \gamma_2 \\ 0 & , \text{otherwise} \end{cases}$$

where $\gamma_1 = R\theta_1$ and $\gamma_2 = R\theta_2$ and θ_1, θ_2 denote the angles subtended by the patch. The longitudinal and transverse displacements, which are coupled due to the curvature, are respectively denoted by v and w.

Under the assumptions of linear displacements, negligible rotational effects and shear deformation, and

4

linear stress-strain relations, force and moment balancing yields the static equations

(4.2)
$$-\frac{1}{R}\frac{dN_\theta}{d\theta} = \hat{q}_\theta$$
$$-\frac{1}{R^2}\frac{d^2 M_\theta}{d\theta^2} + \frac{1}{R}N_\theta = \hat{q}_n - \frac{1}{R^2}\frac{d^2 \widehat{M}_\theta}{d\theta^2}.$$

Here N_θ and M_θ denote the internal force and moment resultants and $\widehat{M}_\theta$ represents the external moment generated by applied voltages to the patches. Finally, $\hat{q}_\theta$ and $\hat{q}_n$ respectively denote applied longitudinal and normal loads to the actuator. As detailed in [1], the modeling equations (4.2) are consistent with the restriction of modified Donnell-Mushtari shell equations to the actuator geometry.

The internal resultants incorporate the material properties of the backing material and PZT and, as derived in [1], are given by

(4.3)
$$N_\theta = Eh\left(\frac{1}{R}\frac{dv}{d\theta} + \frac{w}{R}\right) + E_{pe}\left[\frac{h_{pe}}{R}\left(\frac{dv}{d\theta} + w\right) - \frac{a_2}{2R^2}\frac{d^2 w}{d\theta^2}\right]\chi_{pe}(\theta)$$
$$M_\theta = \frac{-Eh^3}{12R^2}\frac{d^2 w}{d\theta^2} + E_{pe}\left[\frac{a_2}{2R}\left(\frac{dv}{d\theta} + w\right) - \frac{a_3}{3R^2}\frac{d^2 w}{d\theta^2}\right]\chi_{pe}(\theta)$$

where $a_2 \equiv (h/2 + h_{pe})^2 - (h/2)^2$ and $a_3 \equiv (h/2 + h_{pe})^3 - (h/2)^3$.

For low to moderate drive regimes in which the linear piezoelectric equations are sufficiently accurate, the external moment generated by the PZT in response to an applied voltage V is

(4.4)
$$\widehat{M}_\theta = \frac{-E_{pe}d_{31}}{2}V(h + h_{pe})\chi_{pe}(\theta)$$

where d_{31} is the linear piezoelectric constant.

We note that the model (4.2), with resultants given by (4.3) and (4.4), neglects material contributions due to the LaRC-SI. If desired, these contributions can be incorporated in the manner described in [1]. We also note that in the strong form (4.2), differentiation of the discontinuous material parameters and patch inputs yields unbounded components in the model. This necessitates the consideration of an appropriate weak form of the model. As a prelude, however, it is necessary to specify appropriate boundary conditions.

We consider four sets of boundary conditions which model the constraints commonly employed in experiments: fixed-end, pinned-end, sliding-end and free-end conditions. These boundary conditions can be applied at either end of the beam; to simplify the discussion, we summarize them at the left end ($\theta = 0$) and note that similar expression hold at $\theta = L$.

(i) Fixed-End Conditions

(4.5)
$$v(0) = 0$$
$$w(0) = \frac{dw}{d\theta}(0) = 0$$

(ii) Pinned-End Conditions

(4.6)
$$v(0) = 0$$
$$w(0) = M_\theta(0) = 0$$

5

(iii) Sliding-End Conditions

$$w(0) = v(0) \tan(\phi_i)$$

(4.7)
$$M_\theta(0) = 0$$

$$N_\theta(0) = -Q_\theta(0) \tan(\phi_c)$$

(iv) Free-End Conditions

(4.8)
$$N_\theta(0) = M_\theta(0) = 0$$

In the sliding end condition, Q_θ denotes the shear force resultant and ϕ_i, ϕ_c respectively denote the initial angle of the actuator and the angle obtained after a load is applied (see Figure 4.1). It can be noted that to within a first-order approximation, ϕ_i and ϕ_c are related by the expression $\phi_c = \phi_i + \frac{dw}{d\theta}$. Finally, for implementation purposes, it has been observed that physically reasonable results can be obtained with the approximation $Q_\theta = 0$ which is typically enforced in first-order shell theory. This yields the natural boundary condition $N_\theta = 0$ which is easily implemented.

We note that care must be exhibited when specifying boundary conditions at the left and right ends of the actuator to ensure model well-posedness. For example, the specification of free-end conditions at both $x = 0$ and $x = L$ will yield rigid body modes and hence will not enforce unique solutions since solutions differing by a constant will be equivalent. For the experiments reported in Section 6, fixed-end conditions were enforced at $x = 0$ and sliding-end conditions were employed at $x = L$.

To accommodate the discontinuities due to the patch and to reduce smoothness requirements on the basis functions employed for numerical approximation, we consider corresponding weak forms of the modeling system. The state space is taken to be $X = L^2(\Omega) \times L^2(\Omega)$ where $\Omega = [0, L]$. The test functions depend upon the boundary conditions under consideration. For fixed, pinned, or sliding-end boundary conditions at $\theta = 0$ and free-end conditions at $\theta = L$, we respectively employ the spaces

(4.9)
$$V = \{(\phi, \varphi) \in H^1 \times H^2 \mid \phi(0) = 0, \varphi(0) = \varphi'(0) = 0\}$$

$$V = \{(\phi, \varphi) \in H^1 \times H^2 \mid \phi(0) = 0, \varphi(0) = 0\}$$

$$V = \{(\phi, \varphi) \in H^1 \times H^2 \mid \varphi(0) = \phi(0) \tan(\phi_i)\}.$$

We note that the constraints $M_\theta(L) = N_\theta(L) = 0$ are natural boundary conditions which do not require any restriction of the underlying Sobolev spaces. Analogous definitions are employed when considering other combinations of boundary conditions.

A weak form of the model is then

(4.10)
$$\int_0^L \left\{ \frac{1}{R} N_\theta \frac{d\phi}{d\theta} - \hat{q}_\theta \phi \right\} d\theta = 0$$

$$\int_0^L \left\{ \frac{1}{R} N_\theta \varphi - \frac{1}{R^2} M_\theta \frac{d^2\varphi}{d\theta^2} - \hat{q}_n \varphi + \frac{1}{R^2} \widehat{M_\theta} \frac{d^2\varphi}{d\theta^2} \right\} d\theta = 0$$

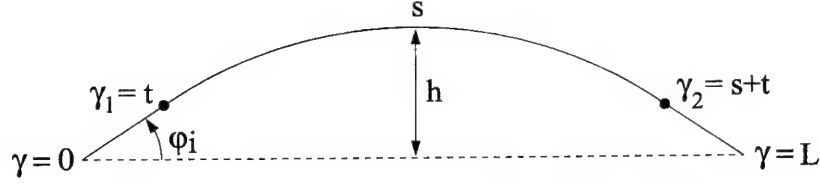for all (ϕ, φ) in the appropriate space V.

FIG. 4.1. *Geometry and arclengths of the composite actuator.*

4.2. Model 2. A second model is derived under the assumption that the actuator region covered by the patch is curved while the tabs are initially straight. This model is constructed by coupling flat and curved beam models through appropriate interface conditions.

To specify the geometry, we let γ denote the arclength with $\gamma = 0$ at the left end of the actuator as depicted in Figure 4.1. We assume that the tabs have equal length t and that the portion covered by the piezoceramic patch has arclength $s = (\theta_2 - \theta_1)R$. The region covered by the patch is denoted by $\Omega_{pe} = [\gamma_1, \gamma_2] = [t, s + t]$ while $\Omega = [0, L]$ again denotes the domain for the full actuator. The characteristic function χ_{pe}, defined in (4.1) delineates that portion of the structure covered by the patch. For the tabs, the arclength is designated by $\gamma = x$ whereas it has the form $\gamma = R\theta$ in the curved portion of the actuator.

For the curved portion of the actuator, force and moment balancing again yield the coupled relations

$$(4.11) \qquad \begin{aligned} -\frac{1}{R}\frac{dN_\theta}{d\theta} &= \hat{q}_\theta \\ -\frac{1}{R^2}\frac{d^2 M_\theta}{d\theta^2} + \frac{1}{R}N_\theta &= \hat{q}_n - \frac{1}{R^2}\frac{d^2 \widehat{M_\theta}}{d\theta^2} \, . \end{aligned}$$

where N_θ, M_θ and $\widehat{M_\theta}$ are defined in (4.3) and 4.4). The tabs have infinite radius of curvature which yields the uncoupled relations

$$(4.12) \qquad -\frac{dN_x}{dx} = \hat{q}_x \quad , \quad -\frac{d^2 M_x}{dx^2} = \hat{q}_n$$

where the resultants are given by

$$(4.13) \qquad N_x = Eh\frac{dv}{dx} \quad , \quad M_x = -\frac{Eh^3}{12}\frac{d^2 w}{dx^2} \, .$$

Finally, the displacements and slopes at γ_1 and γ_2 are coupled through the interface constraints

$$(4.14) \qquad \begin{aligned} \lim_{\gamma \to \gamma_1^-} v(\gamma) &= \lim_{\gamma \to \gamma_1^+} v(\gamma) &\quad , \quad \lim_{\gamma \to \gamma_2^-} v(\gamma) &= \lim_{\gamma \to \gamma_2^+} v(\gamma) \\ \lim_{\gamma \to \gamma_1^-} w(\gamma) &= \lim_{\gamma \to \gamma_1^+} w(\gamma) &\quad , \quad \lim_{\gamma \to \gamma_2^-} w(\gamma) &= \lim_{\gamma \to \gamma_2^+} w(\gamma) \\ \lim_{\gamma \to \gamma_1^-} \frac{dw}{dx}(\gamma) &= \lim_{\gamma \to \gamma_1^+} \frac{dw}{dx}(\gamma) &\quad , \quad \lim_{\gamma \to \gamma_2^-} \frac{dw}{dx}(\gamma) &= \lim_{\gamma \to \gamma_2^+} \frac{dw}{dx}(\gamma) \, . \end{aligned}$$

Formulation of the model in terms of the arclength γ yields the unified relations

$$(4.15) \qquad \begin{aligned} -\frac{dN_\gamma}{d\gamma} &= \hat{q}_\gamma \\ -\frac{d^2 M_\gamma}{d\gamma^2} + \frac{1}{R}N_\gamma &= \hat{q}_n - \frac{d^2 \widehat{M_\gamma}}{d\gamma^2} \, . \end{aligned}$$

7

with

$$N_\gamma = Eh \left(\frac{dv}{d\gamma} + \frac{w}{R} \right) + E_{pe} \left[h_{pe} \frac{dv}{d\gamma} + \frac{h_{pe} w}{R} - \frac{a_2}{2} \frac{d^2 w}{d\gamma^2} \right] \chi_{pe}(\gamma)$$

(4.16)
$$M_\gamma = \frac{-Eh^3}{12} \frac{d^2 w}{d\gamma^2} + E_{pe} \left[\frac{a_2}{2} \frac{dv}{d\gamma} + \frac{a_2 w}{2R} - \frac{a_3}{3} \frac{d^2 w}{d\gamma^2} \right] \chi_{pe}(\gamma)$$

$$\widehat{M}_\gamma = \frac{-E_{pe} d_{31}}{2} V(h + h_{pe}) \chi_{pe}(\gamma).$$

The radius of curvature is taken to be $R = \infty$ for the tabs. When employing the formulation (4.15), it must be noted that the second derivatives may not exist at the points γ_1 and γ_2. Finally, fixed, pinned and sliding-end boundary conditions are enforced by employing the constraints (4.5) - (4.7) at $\gamma = 0$ or $\gamma = L$.

The construction of the weak model formulation is analogous to Model 1 with the exception that second derivatives of the transverse test functions may not exist at the interface points $[\gamma_1, \gamma_2]$. To illustrate, the space of test functions for an actuator with fixed-end conditions at $\gamma = 0$ and sliding-end conditions at $\gamma = L$ is

$$V = \Bigg\{ (\phi, \varphi) \in H^1 \times H^2 \mid \phi(0) = 0, \varphi(0) = \varphi'(0) = 0, \varphi(L) = \phi(L) \tan(\phi_i) \text{ and}$$

$$\lim_{\gamma \to \gamma_1^-} \varphi''(\gamma) \neq \lim_{\gamma \to \gamma_1^+} \varphi''(\gamma), \lim_{\gamma \to \gamma_2^-} \varphi''(\gamma) \neq \lim_{\gamma \to \gamma_2^+} \varphi''(\gamma) \Bigg\}.$$

Analogous spaces are employed for the remaining combinations of boundary conditions. A weak form of the model is then

(4.17)
$$\int_0^L \left\{ N_\gamma \frac{d\phi}{d\gamma} - \hat{q}_\gamma \phi \right\} d\gamma = 0$$

$$\int_0^L \left\{ -M_\gamma \frac{d^2 \varphi}{d\gamma^2} + \frac{1}{R} N_\gamma \varphi - \hat{q}_n \varphi + \widehat{M}_\gamma \frac{d^2 \varphi}{d\gamma^2} \right\} d\gamma = 0$$

for all $(\phi, \varphi) \in V$.

5. Numerical Approximation Techniques. To approximate the solution of (4.10) or (4.17), we consider Galerkin techniques with basis functions chosen to satisfy smoothness requirements as well as boundary and interface conditions. We consider first the system which arises when discretizing the model for the uniformly curved actuator.

5.1. Model 1. We consider Galerkin approximation for v and w which are respectively based on linear and cubic Hermite functions. To define the bases, consider a uniform partition of $[0, L]$ with gridpoints $\theta_i = ih, h = L/N, i = 0, \cdots, N$. For $i = 1, \cdots, N-1$, linear splines are taken to be

(5.1)
$$\phi_i(\theta) = \frac{1}{h} \begin{cases} (\theta - \theta_{i-1}) & , \quad \theta \in [\theta_{i-1}, \theta_i] \\ (\theta_{i+1} - \theta) & , \quad \theta \in [\theta_i, \theta_{i+1}] \\ 0 & , \quad \text{otherwise}. \end{cases}$$

The cubic Hermite basis functions employed to specify w and w' are given by

$$\varphi_{i0}(\theta) = \frac{1}{h^3} \begin{cases} (\theta - \theta_{i-1})^2 [2(\theta_i - \theta) + h] & , \quad \theta \in [\theta_{i-1}, \theta_i] \\ (\theta_{i+1} - \theta)^2 [2(\theta_{i+1} - \theta) - h] & , \quad \theta \in (\theta_i, \theta_{i+1}] \\ 0 & , \quad \text{otherwise} \end{cases}$$

and

$$\varphi_{i1}(\theta) = \frac{1}{h^2} \begin{cases} (\theta - \theta_{i-1})^2(\theta - \theta_i) & , \quad \theta \in [\theta_{i-1}, \theta_i] \\ (\theta_{i+1} - \theta)^2(\theta - \theta_i) & , \quad \theta \in (\theta_i, \theta_{i+1}] \\ 0 & , \quad \text{otherwise} \,. \end{cases}$$

As detailed in [11], all three sets of basis functions vanish identically outside the interval $[\theta_{i-1}, \theta_{i+1}]$. The basis functions $\phi_0, \varphi_{00}, \varphi_{01}$ and $\phi_N, \varphi_{N0}, \varphi_{N1}$ are defined similarly on the intervals $[0, \theta_1]$ and $[\theta_{N-1}, \theta_N]$ (see [11, pages 49 and 57]). The essential boundary conditions (i)-(iii) summarized in (4.5)-(4.7) are enforced by omitting or forming linear combinations of the boundary basis functions.

The displacements are then represented as linear combinations of basis functions with coefficients determined by enforcing the constraints provided by the weak form of the model. To illustrate, consider the discretization of the model satisfying fixed-end conditions at $\theta = 0$ and pinned-end conditions at $\theta = L$. The approximate solutions are taken to be

(5.2)
$$v^N(\theta) = \sum_{j=1}^{N-1} v_j \phi_j(\theta)$$
$$w^N(\theta) = \sum_{j=1}^{N-1} w_j \varphi_{j0}(\theta) + \sum_{j=1}^{N} \widetilde{w}_j \varphi_{j1}(\theta)$$

in the subspace $H^N \subset V$. Analogous expressions are employed for other combinations of boundary conditions.

A matrix system is obtained by considering the approximate solution in (4.10) with basis functions employed as test functions (this is equivalent to projecting the system (4.10) onto the finite dimensional subspace H^N). This yields the linear relation

(5.3)
$$K\vec{v} = \vec{f}$$

where $\vec{v} = [v_1, \cdots, v_{N-1}, w_1, \cdots, w_{N-1}, \widetilde{w}_1, \cdots, \widetilde{w}_N]$ denotes the vector of unknown coefficients.

5.2. Model 2. The formulation of approximation techniques for Model 2 is accomplished in a similar manner. In this case, we consider uniform partitions on each of the subintervals $[0, \gamma_1], [\gamma_1, \gamma_2], [\gamma_2, L]$ and define basis functions on each subdomain. The displacements $v^N = [v_1^N, v_2^N, v_3^N]$ and $w^N = [w_1^N, w_2^N, w_3^N]$ are defined in a manner analogous to (5.2) with the interface conditions enforced through the constraints

$$v_1^N(\gamma_1) = v_2^N(\gamma_1) \qquad , \quad v_2^N(\gamma_2) = v_3^N(\gamma_2)$$

$$w_1^N(\gamma_1) = w_2^N(\gamma_1) \qquad , \quad w_2^N(\gamma_2) = w_3^N(\gamma_2)$$

$$\frac{dw_1^N}{d\gamma}(\gamma_1) = \frac{dw_2^N}{d\gamma}(\gamma_1) \quad , \quad \frac{dw_2^N}{d\gamma}(\gamma_2) = \frac{dw_3^N}{d\gamma}(\gamma_2)$$

Orthogonalization against the test functions then yields a corresponding linear system

$$K\vec{v} = \vec{f}$$

which can be solved to obtain the displacement and slope coefficients at each of the nodes in the subdomains.

6. Experimental Validation. In this section, we illustrate the performance of the combined model through comparison with experimental data. In the first example, the strain model outlined in Section 3 is used to predict the shape of a variety of actuators as a function of the manufacturing process. This provides the initial geometry employed in Section 4 when characterizing displacements generated through voltage inputs to the patches. The performance of the displacement model is illustrated in Example 2.

6.1. Example 1. Actuator Shape

The model summarized in Section 3 quantifies the thermal and electrostatic strains and resulting changes in curvature generated during the cooling and repoling of the actuator during the manufacturing process. This provides a means of characterizing the radius of curvature and dome height for an actuator as functions of properties of the constituent materials as well as the dimensions of these materials. We consider in this example an actuator construction comprised of a stainless steel bottom layer, LaRC-SI, PZT-5A and a protective LaRC-SI top layer (there is no metallic top layer). The width of all materials was 0.5 inches and the PZT was 1.5 inches in length while the stainless steel was 2.5 inches in length. Hence $s = 1.5$ and $t = 0.5$ in Figure 4.1. The PZT was 8 mils thick while the LaRC-SI had a mean thickness of 1 mil. Actuators were constructed with steel thicknesses ranging from 1 mil to 20 mils to illustrate the effect of backing material thickness on the final dome height of the actuator. Note that the dimensions of the THUNDER devices considered here permit the use of the 1-D model.

The dome heights h predicted by the relation (3.1) are compared with experimental data from actuators having steel thicknesses ranging from 3 mils to 20 mils in Figure 6.1. In the model, the parameter values $E_{pe} = 177 \times 10^9$ N/m^2, $E_{SI} = 7.45 \times 10^9$ N/m^2, $E_{steel} = 173 \times 10^9$ N/m^2, $\alpha_{pe} = 0.8 \times 10^{-7}$, $\alpha_{SI} = 46 \times 10^{-6}$ (23-150° C), $\alpha_{SI} = 60 \times 10^{-6}$ (23-150° C), $\alpha_{steel} = 9.8 \times 10^{-6}$, $\lambda_s = 0.6 \times 10^{-3}$ and $\nu = 0.3$ were estimated through a least squares fit to the full data set. It is observed that the model predicts both the trends and magnitudes for the dome heights to within 5% relative accuracy for all steel thicknesses except 6 mils for which the relative error was 8%. This provides a characterization of the actuator shape which can then be employed when modeling subsequent displacements or forces.
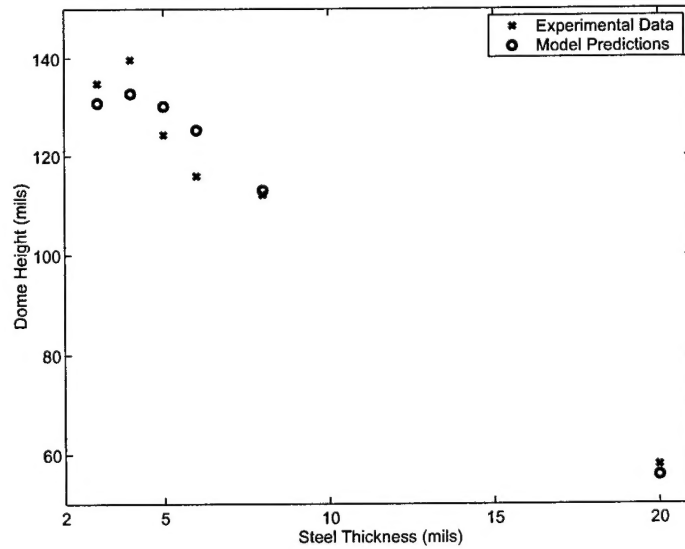

FIG. 6.1. *Model predictions and experimentally measured dome heights h as a function of steel thickness.*

6.2. Example 2:. Actuator Displacements

To illustrate the performance of the displacement model presented in Section 4, we consider the construction described in Example 1 for actuators having fixed-end conditions at the left edge ($\gamma = 0$) and sliding-end conditions at the right edge ($\gamma = L$). Model 2 was used to predict the displacements generated at the patch center ($\gamma = t + s/2$) for a variety of steel thicknesses and input voltages.

For fixed voltage levels, model predictions for the displacement to voltage ratio as a function of steel thickness are compared with experimental data in Figure 6.2a. It is observed that the model accurately predicts the displacement for actuators having steel thicknesses of 3 mils, 8 mils and 10 mils with discrepancies observed at 1 mil and 6 mils. We note that the LaRC-SI has the same thickness as the steel at 1 mil and we hypothesize that in this case, unmodeled viscoelastic properties of the LaRC-SI may be dominating the elastic properties of the steel. The error in the 6 mil prediction reflects the discrepancy observed in the dome height prediction for that thickness.

To further illustrate the performance of the model at low drive levels, the predicted displacements for input voltage levels of 20 V, 80 V and 120 V are compared with experimentally measured displacements in Figure 6.2b. The steel thickness in this case was 10 mil. It is observed that within this (approximately) linear range, the model accurately predicts the displacement for a variety of input levels.

7. Concluding Remarks. The model described here provides a technique for quantifying both the initial shape of THUNDER devices due to the manufacturing process and displacements generated by applied voltages. The actuator shapes were modeled through the quantification of thermal and electrostatic strains while Newtonian principles were used to derive PDE models characterizing displacements for a variety of boundary conditions and exogenous loads. Both components of the model were illustrated through comparison with experimental data.

It should be noted that linear theory was employed when deriving both components of the model and degradation of performance is expected in high drive regimes. The extension of both components to nonlinear regimes is under current investigation. The extension of the thermal model to include nonlinear effects is being considered in the context of theory in [10]. To incorporate the constitutive nonlinearities and hysteresis inherent to piezoceramic materials at moderate to high drive levels, the models developed in [12, 13] are
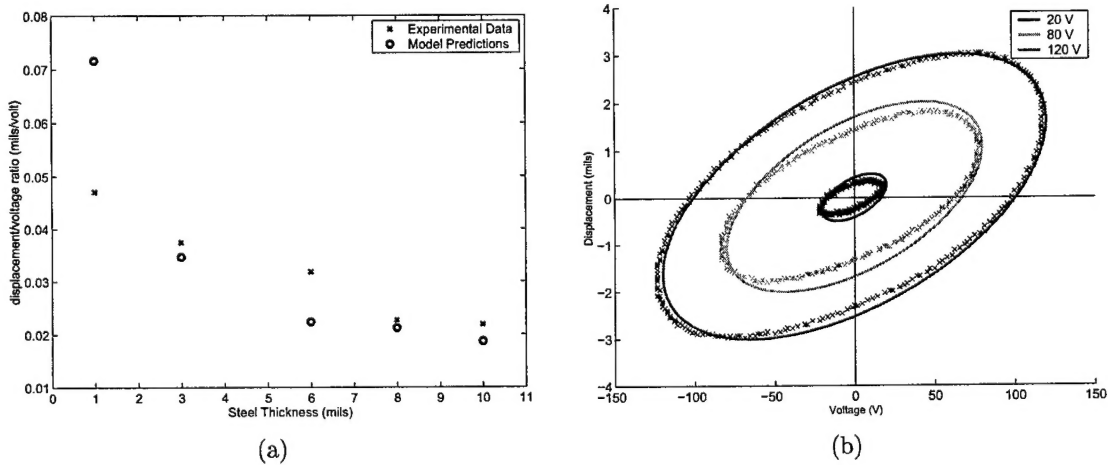

Fɪɢ. 6.2. *(a) Model predictions and measured displacements as a function of steel thickness; (b) Modeled and measured displacements as a function of input voltage: xxxx (Data),* ——— *(Model).*

being combined with the current model to accommodate large inputs. Finally, nonlinear shell theory will be employed to ascertain limitations in the linear PDE presented here when displacements are large.

REFERENCES

[1] H.T. BANKS, R.C. SMITH AND Y. WANG, *Smart Material Structures: Modeling, Estimation and Control*, Masson/John Wiley, Paris/Chichester, 1996.

[2] B.A. BOLEY AND J.H. WEINER, *Theory of Thermal Stresses*, John Wiley and Sons, New York, 1960.

[3] M. CAPOZZOLI, J. GOPALAKRISHNAN, K. HOGAN, J. MASSAD, T. TOKARCHIK, S. WILMARTH, H.T. BANKS, K.M. MOSSI AND R.C. SMITH, *Modeling Aspects Concerning THUNDER Actuators*, Proceedings of the SPIE, Smart Structures and Materials 1999, Volume 3667, 1999, pp. 719-727.

[4] D.L. EDBERG, *Control of flexible structures by applied thermal gradients*, AIAA Journal, 25(6) (1987), pp. 877-883.

[5] A. HAMAMOTO AND M.W. HYER, *Nonlinear temperature-curvature relationships for unsymmetric graphite epoxy laminates*, International Journal of Solids and Structures, 23(7) (1987), pp. 919-935.

[6] M.W. HYER, *The room-temperature shapes of four-layer unsymmetric cross-ply laminates*, Journal of Composite Materials, 16(4) (1981), pp. 318-340.

[7] M.W. HYER AND A. JILANI, *Predicting the deformation characteristics of rectangular unsymmetrically laminated piezoelectric materials*, Smart Materials and Structures, 7 (1998), pp. 1-8.

[8] B. JAFFE, W.R. COOK, JR. AND H. JAFFE, *Piezoelectric Ceramics*, Academic Press, New York, 1971.

[9] A.J. MOULSON AND J.M. HERBERT, *Electroceramics*, Chapman and Hall, New York, 1990.

[10] A. NADAI, *Theory of Flow and Fracture of Solids*, Volume 2, McGraw-Hill, New York, 1963.

[11] P.M. PRENTER, *Splines and Variational Methods*, Wiley Classics Edition, New York, 1989.

[12] R.C. SMITH AND C.L. HOM, *Domain wall theory for ferroelectric hysteresis*, Journal of Intelligent Material Systems and Structures, 10(3) (1999), pp. 195-213.

[13] *R.C. Smith and Z. Ounaies, A domain wall model for hysteresis in piezoelectric materials*, Journal of Intelligent Material Systems and Structures, 11(1) (2000), pp. 62-79.

[14] B.K. TALEGHANI AND J.F. CAMPBELL, *Nonlinear finite element modeling of THUNDER piezoelectric actuators*, NASA report NASA/TM-1999-209322, 1999.